

Banner appropriate to article type will appear here in typeset article

Triangular instability of a strained Lamb-Oseen vortex

A. S. P. Ayapilla^{1†}, Y. Hattori² and S. Le Dizès³

¹Graduate School of Information Sciences, Tohoku University, Sendai 980-8579, Japan

²Institute of Fluid Science, Tohoku University, Sendai 980-8577, Japan

³Aix Marseille Université, CNRS, Centrale Méditerranée, IRPHE, Marseille, France

(Received xx; revised xx; accepted xx)

In this study, we demonstrate, for the first time, the existence of a short-wave instability in a Lamb-Oseen vortex subjected to a triangular strain field generated by three satellite vortices, which we term the triangular instability. We identify this instability by numerically integrating the linearized Navier-Stokes equations around a quasi-steady base flow to capture the most unstable mode and validate it by comparing results with theoretical predictions. We evaluate this instability by calculating the growth rates associated with the parametric resonant coupling of two Kelvin waves with the triangular strain field in the limit of small strain rate and large Reynolds number. Our analysis reveals that resonance occurs only for combinations of the azimuthal wavenumbers $m = 1$ and $m = -2$ (or their symmetric counterparts with opposite signs). We observe several unstable modes with positive growth rates for a moderate viscous Reynolds number of 10^4 and a straining parameter value of $\epsilon = 0.008$, defined as the cube of the ratio of the core size to the distance from the satellite vortices. The most unstable mode arises at the crossing point of the second branch of the dispersion curves for $m = 1$ and the first branch for $m = -2$. This mode, with an axial wavenumber $k \approx 5.18/a$ and frequency $\omega \approx -0.312\Omega$ (a and Ω represent the core size and the angular velocity at the center, respectively), exhibits the largest growth rate, persisting across varied Reynolds numbers and ϵ values, and suffers negligible critical layer damping.

1. Introduction

Vortices are a common phenomenon in fluid motion, occurring at scales ranging from the tiny vortices in a cup of coffee to the massive Great Red Spot on Jupiter. The study of vortex dynamics has been a central area of research since the 19th century, pioneered by Helmholtz and Lord Kelvin, and later advanced through the contributions of Saffman and other researchers in fluid dynamics and applied mathematics. The fundamental concepts in this field are comprehensively outlined in Saffman's renowned book, "Vortex Dynamics" (Saffman 1995). A particularly significant aspect of vortices is their susceptibility to instabilities, which can arise from interactions with their surroundings or within the vortices themselves. In recent decades, extensive research has been conducted on vortex stability, with particular focus on vortex pairs, which are crucial in the context of aircraft trailing wakes and their amplification. An extensive summary of the general stability study of vortices can be found in

† Email address for correspondence: ayapilla.aditya.sai.pranith.t6@dc.tohoku.ac.jp

Ash *et al.* (1995), and the advancements in the study of vortex pair dynamics and instabilities have been thoroughly reviewed by Leweke *et al.* (2016). Such studies have also been essential for understanding how turbulence arises from instabilities caused by eddy interactions and the dynamics of coherent structures within turbulent flows (Pullin & Saffman 1998).

Vortex pairs are known to experience two main types of instabilities: long-wave and short-wave instabilities. These are often referred to as cooperative instabilities, as they primarily result from the interaction between the vortices within the pair. They are also three-dimensional in nature. Long-wave instability, also known as Crow instability, occurs at scales much larger than the size of the vortex core. It was discovered by Crow (1970) for a vortex pair. More studies about the long-wave instabilities can be found in Brion *et al.* (2007), Leweke & Williamson (2011), and similar works. It is often observed in the sky, affecting the contrails of aircraft flying at high altitudes.

In contrast, short-wave instability occurs at scales comparable to or smaller than the vortex core. Moore & Saffman (1975) and Tsai & Widnall (1976) were the first to discover and explain the mechanism of this instability. It is understood to occur because the streamlines of the vortex undergo elliptic deformation due to the strain induced by the adjacent vortex, causing two Kelvin waves (small perturbations) with specific azimuthal wavenumber combinations to resonate with the strain and become unstable. Due to the elliptic nature of the streamline deformation, this is also referred to as elliptic instability and is sometimes known as the Moore-Saffman-Tsai-Widnall (MSTW) instability. An extensive summary on the elliptic instability can be found in Kerswell (2002), and some important original contributions include Pierrehumbert (1986), Bayly (1986), Leweke & Williamson (1998), Le Dizès & Laporte (2002), Meunier & Leweke (2005), Schaeffer & Le Dizès (2010), etc. The modes with $m = 1$ and $m = -1$, also known as stationary helical modes, were found to be the most unstable.

Tsai & Widnall (1976) analyzed the Rankine vortex, while Moore & Saffman (1975) focused on the Lamb-Oseen vortex. For the Rankine vortex, the eigenvalue problem for linearized disturbances on the unstrained vortex can be solved analytically, yielding the eigenmodes and eigenfunctions of the Kelvin waves. These eigenfunctions are expressed in terms of Bessel functions (Tsai & Widnall 1976; Saffman 1995; Fukumoto 2003). However, for the Lamb-Oseen and Batchelor vortices, obtaining explicit analytical expressions for the eigenfunctions is not possible. Nevertheless, their asymptotic forms can be derived in the limit of large k , as shown by Le Dizès & Lacaze (2005). Using the Wentzel-Kramers-Brillouin (WKB) approach, they provided approximate analytical expressions for the dispersion relation and eigenmodes and discussed the conditions for the existence of regular neutral core and ring modes. Sipp & Jacquin (2003), Fabre *et al.* (2006) solved the problem numerically using a Chebyshev spectral collocation method. Their findings revealed that many eigenmodes are suppressed due to critical layer damping, which arises due to the smooth distribution of vorticity. Additionally, Eloy & Le Dizès (2001) performed a detailed stability analysis of the Rankine vortex, identifying resonant combinations beyond the helical modes. Their analysis was also extended to consider a multipolar straining field.

Another type of short-wave instability was found to occur theoretically in vortex rings by Hattori & Fukumoto (2003) and Fukumoto & Hattori (2005). It was caused by the inherent curvature of the vortex rings and occurred for combinations of azimuthal wavenumbers differing by one. The authors conducted stability analyses on the Rankine vortex to deduce the characteristics of curvature instability. Blanco-Rodríguez & Le Dizès (2017) theoretically computed the growth rates for a Batchelor vortex, and, along with Blanco-Rodríguez & Le Dizès (2016), demonstrated that curvature also contributes to elliptic instability. Hattori *et al.* (2019) further confirmed curvature instability in a vortex ring with swirl through numerical stability analysis using DNS. Recently, Xu *et al.* (2025) proposed a numerical

procedure to study instabilities in helical vortex systems and showed that curvature instability is also present in such systems.

Although elliptic and curvature instabilities have been extensively studied over the past few decades, much less attention has been given to multipolar instabilities, particularly triangular instabilities. The only studies on triangular instability have been conducted for the Rankine vortex (Eloy *et al.* 2000; Eloy & Le Dizès 2001; Eloy *et al.* 2003), and there are no theoretical or numerical studies confirming the existence of triangular instability for Lamb-Oseen or Batchelor vortices. The existence of triangular instability in more realistic vortices like the Lamb-Oseen and Batchelor vortices could have significant implications and provide valuable insights for engineering applications such as turbomachines with three blades, like ship or aircraft propellers, wind turbines, and more. In such cases, the helical vortices that form around the central hub vortex may induce triangular straining on the hub vortex, potentially triggering instabilities. Additionally, long-lived non-axisymmetric vortices, such as dipoles, tripoles, and higher-order multipolar structures, have been observed in rotating turbulent flows through experiments and direct numerical simulations (Hopfinger & Van Heijst 1993; Carnevale & Kloosterziel 1994; Rossi *et al.* 1997; Dritschel 1998). Kelvin waves have also been identified on vortex filaments in transitional flows (Arendt *et al.* 1998), with elliptic and multipolar instabilities potentially explaining the emergence and growth of these waves.

In this study, we aim to investigate the stability of a Lamb-Oseen vortex under triangular straining to short-wave instabilities through the parametric resonance of Kelvin waves. This is achieved by conducting a linear stability analysis using both direct numerical simulations (DNS) and theoretical analysis. Our objectives include computing and comparing the growth rates and structures of the unstable modes (if present) obtained through a linearized DNS and theoretical analysis. Non-linear effects are not considered in this work. Although the simulations we conduct are linearized DNS, we will refer to them simply as DNS for brevity. In the DNS approach, we first determine the base flow and then integrate the linearized Navier-Stokes equations to identify the most unstable mode. In the theoretical analysis, we derive an approximation for the base flow under the assumption of a weak triangular straining field and use this approximation to derive linear perturbation equations for the strained Lamb-Oseen vortex. These equations are then used to compute the growth rates of the resonant modes. To identify the resonant modes, we solve the eigenvalue problem corresponding to the unperturbed vortex. Further details of the methods and analysis are provided in the subsequent sections.

The paper is structured as follows. In Section 2, we formulate the problem and describe the numerical procedure in detail, both for obtaining the base flow, and performing the linearized DNS to identify the most unstable mode. In Section 3, we derive the base flow using theoretical analysis and outline the procedure for obtaining its analytical expressions. We then compare these theoretical results with those from DNS. In Section 4, we provide a comprehensive explanation of the linear stability analysis, including the linearized perturbation equations and the expressions for the growth rates of the resonant modes. We then compare the results from DNS and theory. Finally, in Section 5, we summarize the key findings of this work and discuss potential future research directions.

2. Numerical procedure

Before delving into the theoretical analysis, we present an outline and detailed description of the numerical procedure used to perform the DNS.

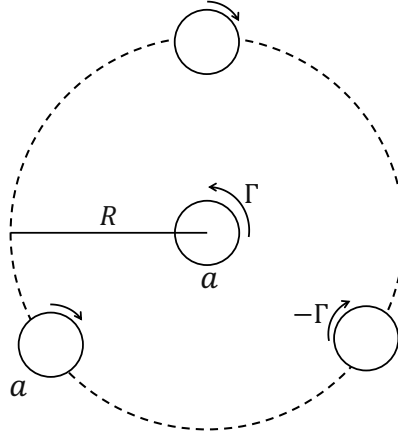


Figure 1: Geometry of the hub vortex and the three satellite vortices

2.1. Outline

As an initial state, we consider a central hub Lamb-Oseen vortex surrounded symmetrically by three satellite Lamb-Oseen vortices in an incompressible, viscous fluid, where the satellite vortices provide triangular straining to the hub vortex, similar to the illustration in figure 1. The satellite vortices are positioned in the vertices of an equilateral triangle, with the hub vortex at its center. If Γ denotes the circulation of the hub vortex, the circulation of each satellite vortex is chosen to be $-\Gamma$. This choice ensures that the velocity induced by the other vortices at the center of any vortex vanishes. As a result, the vortices are not expected to move. In this manner, the system composed of hub and satellite vortices can form a quasi-steady state, the stability of which can be analysed.

2.2. Numerical methods

The numerical analysis will involve two main steps. First, we obtain the quasi-steady base flow by solving the two-dimensional (2-D) Navier-Stokes equations; then, we integrate the linearized Navier-Stokes equations around this base flow over a sufficiently long duration to determine the most unstable mode, if it exists, for a linear disturbance with a specified axial wavenumber, as detailed in the following paragraphs.

The analysis is performed in polar coordinates. The base flow is computed in 2-D (r, θ) , while the linear stability analysis extends to three dimensions (3-D) (r, θ, z) . The linearized Navier-Stokes equations for the disturbances u, v, w and p around a given 2-D base flow (U, V) can be expressed as

$$\begin{aligned} \frac{\partial u}{\partial t} = & -U \frac{\partial u}{\partial r} - \frac{V}{r} \frac{\partial u}{\partial \theta} + \frac{2Vv}{r} - u \frac{\partial U}{\partial r} - \frac{v}{r} \frac{\partial U}{\partial \theta} \\ & - \frac{\partial p}{\partial r} + \frac{1}{Re} \left[\left(\nabla^2 - \frac{1}{r^2} \right) u - \frac{2}{r^2} \frac{\partial v}{\partial \theta} \right], \end{aligned} \quad (2.1)$$

$$\begin{aligned} \frac{\partial v}{\partial t} = & -U \frac{\partial v}{\partial r} - \frac{V}{r} \frac{\partial v}{\partial \theta} - u \frac{\partial V}{\partial r} - \frac{v}{r} \frac{\partial V}{\partial \theta} - \frac{Uv + uV}{r} \\ & - \frac{1}{r} \frac{\partial p}{\partial \theta} + \frac{1}{Re} \left[\left(\nabla^2 - \frac{1}{r^2} \right) v + \frac{2}{r^2} \frac{\partial u}{\partial \theta} \right], \end{aligned} \quad (2.2)$$

$$\frac{\partial w}{\partial t} = -U \frac{\partial w}{\partial r} - \frac{V}{r} \frac{\partial w}{\partial \theta} - \frac{\partial p}{\partial z} + \frac{1}{Re} \nabla^2 w, \quad (2.3)$$

where $\nabla^2 = \partial_r^2 + (1/r)\partial_r + (1/r^2)\partial_\theta^2 + \partial_z^2$. These equations are discretized and solved numerically on the same 2-D grid as the base flow. By assuming periodic boundary conditions in the z -direction, the above equations are separable in the z -direction, which allows us to consider a single wave of the form

$$F(t, r, \theta, z) = e^{ikz} \sum_m \hat{F}_m(t, r) e^{im\theta}$$

for u, v, w and p . The 2-D numerical domain spans $0 \leq r \leq L_r$ and $0 \leq \theta \leq 2\pi$, with $L_r = 1000$. For spatial discretization, we use a sixth-order accurate compact scheme (Lele 1992) in r and a Fourier spectral method in θ , with periodic boundary conditions. Time-marching is achieved through a fourth-order accurate Runge-Kutta method. To avoid the singularity at $r = 0$, we expand the r axis to $-L_r \leq r \leq L_r$ and omit a grid point at $r = 0$. The Poisson equation for the pressure is decomposed into a set of ordinary differential equations for individual Fourier modes, which are also solved with the sixth-order compact scheme. For temporal discretization, we apply the Crank-Nicolson scheme to the viscous terms and the second-order Adams-Bashforth method to the other terms. Further details are provided in appendix A of Hattori *et al.* (2019).

The base flow is obtained once the vortices have equilibrated in the field of the other vortices. This rapid relaxation process has been described in the literature for two vortices (Sipp *et al.* 2000b; Le Dizès & Verga 2002). After equilibrium is reached, the 2-D solution evolves on a slow viscous time scale. This evolution will not be considered further, as we assume a frozen base flow and linearize the Navier-Stokes equations around it. The same numerical methods and discretization used for obtaining the base flow are applied to integrate the frozen linearized Navier-Stokes equations.

2.3. Initial conditions and simulation parameters

The vortices are initially positioned as shown in figure 1. The hub vortex is located at the center of the frame, and the three satellite vortices are placed at a distance of R from the hub vortex center, with an angular separation of $2\pi/3$. Initially, all vortices are assumed to have a Gaussian vorticity profile with a core radius a_i . After the relaxation process, the core size of the vortices has slightly increased to a larger value a . This new core size will be used to non-dimensionalize all spatial variables in the theory. The vortex circulation, however, is conserved. Thus, the Reynolds number Re defined by

$$Re = \frac{\Gamma}{2\pi\nu}, \quad (2.4)$$

where ν is the kinematic viscosity, does not change. We start the simulation with a core size of $a_i = 0.8$ for both hub and satellite vortices and stop it when the core size of the hub vortex reaches $a = 1$, which occurs well after the establishment of a quasi-steady state. The distance between the hub and the satellite vortices, denoted by R , is set to $R = 5$. Unlike the growing core size, this distance remains nearly constant as the base flow reaches a quasi-steady state. Thus, at the quasi-steady state, we have $a = 1$ and $R = 5$. The initial circulation Γ of the hub vortex is set to 2π ($-\Gamma$ for the satellite vortices). We tracked the circulation, first-order, and second-order moments of the vorticity field of the hub vortex throughout the simulation, which allowed us to compute its core radius and keep track of how it changes with time. The details of these calculations are provided in appendix A.

In the simulations, we select $Re = 10^3$ to obtain the base flow but choose a larger value $Re = 10^4$ for the perturbation analysis. This large value of the Reynolds number for the perturbation analysis will guarantee the existence of unstable modes. The choice of a smaller value of the Reynolds number for the base flow is just to reach the quasi-steady state of core

size $a = 1$ from $a_i = 0.8$ more rapidly. This is justified because the quasi-steadystate is not expected to depend on the Reynolds number (Le Dizès & Verga (2002)). The most unstable mode for a given axial wavenumber k , if it exists, is obtained by DNS from a random vorticity initial condition. The irrelevant modes decay and the unstable modes grow exponentially, from which the growth rate can be obtained. A non-uniform grid is used where the number of grid points in r is taken to be 695 and the number of fourier modes in θ to be 512. Radial grid spacing of 0.0475 is used in the region of hub vortex and satellite vortices.

3. Base flow: theory and results

In this section, we present the theoretical analysis used to derive the analytical expressions for the base flow, which are then applied in the linear stability analysis. While the numerical simulations consider the full system composed of the hub vortex and the three satellite vortices, the theory focuses on the hub vortex. The objective is to obtain an approximation for the velocity field of the hub vortex in the presence of satellite vortices. Such an analysis has already been performed for a vortex pair (Le Dizès & Verga 2002).

The idea is to obtain an asymptotic solution in the limit of small a/R . For this purpose, we introduce a small parameter $\epsilon = (a/R)^3$, giving us $\epsilon = 0.008$, for the values of a and R at the quasi-steady state. The field induced by the satellite vortices on the hub vortex can then be modelled using a point vortex approximation for the satellite vortices. In the center of the hub vortex, this gives an expression for the induced velocity field that reads, in cartesian coordinates, at leading order, as

$$U_x = -3\epsilon(x^2 - y^2), \quad U_y = 6\epsilon xy, \quad (3.1)$$

and upon transformation into 2-D polar coordinates, we get the components in r and θ as

$$U_r = -3\epsilon r^2 \cos 3\theta, \quad U_\theta = 3\epsilon r^2 \sin 3\theta. \quad (3.2)$$

Thus, (U_r, U_θ) does correspond to a triangular straining field.

In Moffatt *et al.* (1994), Jiménez *et al.* (1996) and Le Dizès (2000), it was theoretically derived and shown how a Lamb-Oseen vortex interacts with a quadrupolar straining field. The interaction with a triangular straining field is similar. We begin by taking a perturbation expansion of the streamfunction $\psi(r, \theta)$ up to $O(\epsilon)$. For the $O(\epsilon)$ term, we assume a normal modes form corresponding to a triangular azimuthal wavenumber (see Section 2. in Le Dizès (2000) for a detailed and a more general derivation). The resulting expression for ψ is substituted in the 2-D inviscid steady-state vorticity equation given by

$$\frac{\partial \zeta}{\partial r} \frac{\partial \psi}{\partial \theta} - \frac{\partial \psi}{\partial r} \frac{\partial \zeta}{\partial \theta} = 0, \quad (3.3)$$

where the vorticity field $\zeta(r, \theta)$ is given by

$$\zeta = -\nabla^2 \psi. \quad (3.4)$$

The approximation of the 2-D velocity field (\bar{U}, \bar{V}) for the triangular-strained Lamb-Oseen vortex can then be obtained from the streamfunction as

$$\bar{U} = \epsilon \frac{3f(r)}{r} \cos 3\theta + O(\epsilon^2), \quad (3.5)$$

$$\bar{V} = r\Omega_0(r) - \epsilon f'(r) \sin 3\theta + O(\epsilon^2), \quad (3.6)$$

where

$$\Omega_0(r) = \frac{(1 - e^{-r^2})}{r^2} \quad (3.7)$$

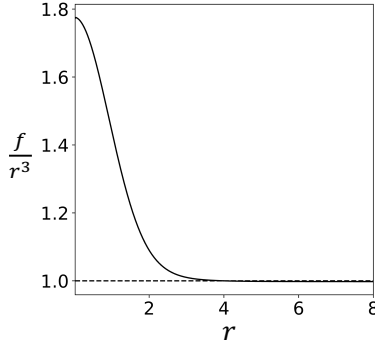


Figure 2: Plot of $f(r)/r^3$ as a function of the radial coordinate r . The value at zero is $s_0 \approx 1.7724$.

is the angular velocity of the Lamb-Oseen vortex, and $f(r)$ a function governed by the following second-order linear ordinary differential equation

$$f'' + r^{-1}f' - \left(9r^{-2} + \frac{4r^2}{(1 - e^{r^2})}\right)f = 0, \quad (3.8)$$

with the boundary conditions,

$$f(r) \sim s_0 r^3, \quad \text{at } r \rightarrow 0, \quad (3.9)$$

$$f(r) \sim r^3, \quad \text{at } r \rightarrow \infty. \quad (3.10)$$

The constant $s_0 \approx 1.7724$ appearing in these equations is a numerical constant derived from the integration of equation (3.8). It corresponds to the amplitude of the straining field in the vortex center, normalized by the amplitude of the straining field at the same point in the absence of the vortex. This ratio corresponds to the value at the origin of the function plotted in figure 2.

The vorticity field of the hub vortex can be written as $\zeta = \zeta_0 + \epsilon \zeta_1 + O(\epsilon^2)$ with

$$\zeta_0 = 2e^{-r^2}, \quad \zeta_1 = g(r) \sin 3\theta, \quad (3.11)$$

with

$$g(r) = \frac{4r^2 f(r)}{1 - e^{r^2}}. \quad (3.12)$$

We compare the DNS-obtained base flow to that derived theoretically to ensure consistency before conducting a linear stability analysis of small disturbances on the base flow. This process involves two steps. First, we verify that a quasi-steady state is reached in DNS by plotting the vorticity field $\zeta(r, \theta)$ and streamfunction $\psi(r, \theta)$ scatter points, where the vorticity and the streamfunction are related via the Poisson's equation $\zeta = -\nabla^2 \psi$. The absence of dispersed regions confirms a quasi-steady state. Such a verification is shown in figure 3. We also calculate the Euler-residue N given by $N = [\langle (\mathbf{u} \cdot \nabla \omega)^2 \rangle / \langle \omega^2 \rangle]^{1/2} \cdot 2\pi R^2 / \Gamma$, which compares the inviscid evolution time scale of the vorticity distribution with the advection time (Sipp *et al.* 2000a). Figure 4 shows the Euler-residue, indicating that the quasi-steady state is reached well before $a = 1$ (marked by the red diamond).

Second, we compare the leading-order and correction terms of the vorticity field, accounting for triangular straining. In figure 5, we show such a comparison for $\epsilon = 0.008$ and

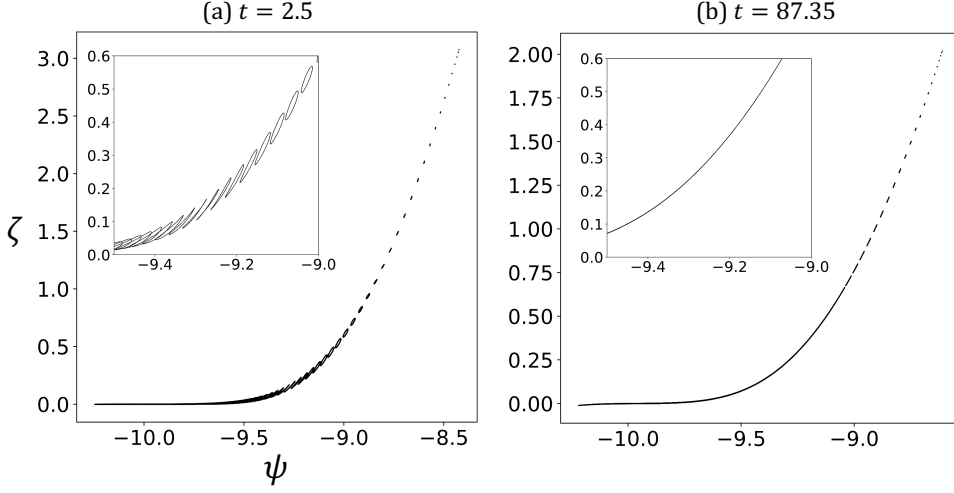


Figure 3: Scatter plot of $\zeta(r, \theta)$ and $\Psi(r, \theta)$ for $Re = 1000$ and $\epsilon = 0.008$; (a) during the relaxation process at $t = 2.5$ and (b) when the core size reaches $a = 1$ at $t = 87.35$ which is well after the establishment of a quasi-steady state. The absence of dispersed regions in (b) indicates that a quasi-steady state has been reached. Zoomed-in regions are included to highlight the differences clearly.

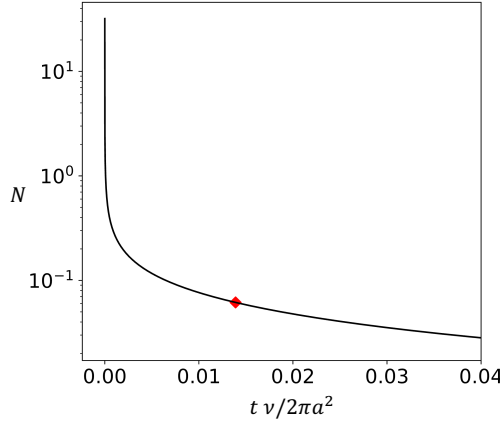


Figure 4: Log-scale plot of Euler-residue N versus t , scaled by viscous time. The red diamond indicates the time when $a = 1$.

270 $Re = 1000$. A good agreement is observed that validates the description of the base flow close
 271 to the hub vortex by equations (3.5)-(3.6). Figure 6(a) displays the streamlines of the base
 272 flow, illustrating the triangular straining effect caused by the three satellite vortices. However,
 273 the distortion near the vortex core remains subtle due to the weak strain ($\epsilon = 0.008$). The
 274 streamfunction, expanded up to first order in ϵ , is given by

$$275 \quad \psi = \psi_0 + \epsilon f(r) \sin(3\theta) + O(\epsilon^2). \quad (3.13)$$

276 The streamlines, to order ϵ , are expressed as

$$277 \quad r = r_0 + \epsilon r_\psi(\theta), \quad (3.14)$$

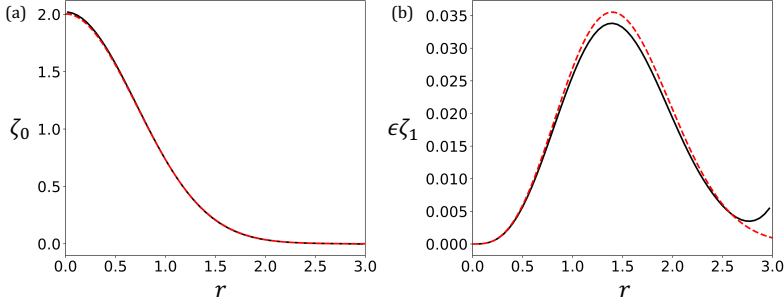


Figure 5: Comparison of the base flow vorticity field obtained with DNS (solid black line) and theory (red dashed line) for $Re = 1000$ and $\epsilon = 0.008$. (a) Leading order term; (b) Correction term due to triangular straining.

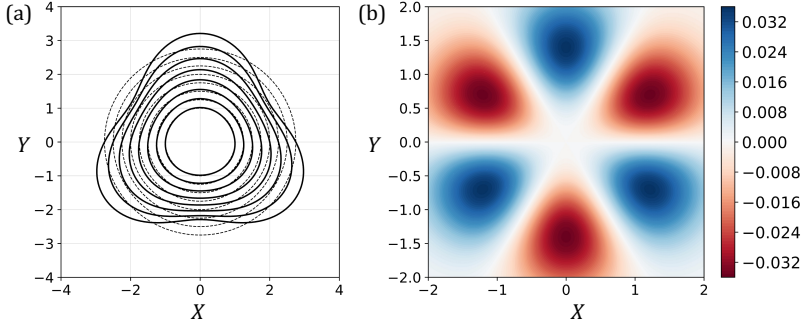


Figure 6: Two-dimensional visualization of the base flow. (a) Streamlines depicted by solid black lines where the streamfunction $\psi = \text{constant}$; plotted from $r_0 = 1$ (innermost contour) to $r_0 = 2.75$ in the intervals of 0.25. The values of ψ starting from $r = 1$ are 2.05, 1.90, 1.74, 1.59, 1.47, 1.35, 1.24, 1.15. The corresponding unstrained streamlines are depicted by dashed lines. (b) Contours of $\epsilon\zeta_1$.

where substituting this into the perturbation expansion for the streamfunction yields

$$r_\psi(\theta) = \frac{f(r_0)}{r_0 \Omega_0(r_0)} \sin(3\theta). \quad (3.15)$$

Here, r_0 represents the streamlines of the unstrained vortex, while $\epsilon r_\psi(\theta)$ quantifies the distortion induced by triangular straining. Figure 6(b) shows the 2D representation of the vorticity field of the base flow, considering only the contribution from the correction term.

4. Linear stability analysis - theory and results

4.1. Perturbation equations of linear disturbances

If one uses expressions (3.5)-(3.6) for the base flow, the linearized Navier-Stokes equations for the velocity-pressure field $\mathbf{u} = (u, v, w, p)$ of the perturbations can be written in the form

$$\left(\mathcal{L} \frac{\partial}{\partial t} + \mathcal{P} \frac{\partial}{\partial z} + \mathcal{M} - \frac{\mathcal{V}}{Re} \right) \mathbf{u} = \epsilon \left(e^{3i\theta} \mathcal{N} + e^{-3i\theta} \overline{\mathcal{N}} \right) \mathbf{u}, \quad (4.1)$$

where the matrices \mathcal{L} , \mathcal{P} , \mathcal{M} , \mathcal{V} , \mathcal{N} are given in appendix B.

4.2. Triangular instability resonance mechanism

The mechanism for the growth of perturbations in a triangular-strained vortex is the same as that for the elliptic instability in the quadripolar-strained vortex (Moore & Saffman 1975; Tsai & Widnall 1976). The only difference is that the triangular strain field corresponds to an azimuthal wavenumber $m = 3$ perturbation of the vortex, while the elliptic strain field corresponds to an $m = 2$ perturbation.

As for the elliptic instability, the instability is associated with a phenomenon of resonance of two quasi-neutral waves of the underlying vortex with the strain field. These waves, also called Kelvin modes, have an expression of the form

$$\mathbf{u} = \tilde{\mathbf{u}}(r)e^{i(m\theta + kz - \omega t)}, \quad (4.2)$$

where m is the azimuthal wavenumber, k the axial wavenumber, ω the frequency, and $\tilde{\mathbf{u}}(r)$ the eigenfunction field of the Kelvin mode. They satisfy the perturbation equations for the unstrained vortex

$$\left(\omega \mathcal{L} - k\mathcal{P} + i\mathcal{M}(m) - \frac{i}{Re}\mathcal{V}(m, k) \right) \tilde{\mathbf{u}} = 0, \quad (4.3)$$

where $\mathcal{M}(m)$ and $\mathcal{V}(m, k)$ are obtained by replacing $\partial/\partial\theta$ with im and $\partial/\partial z$ with ik , in the matrix operators \mathcal{M} and \mathcal{V} , given in appendix B.

To get the possible coupling of two Kelvin modes with the strain field, one should find two neutral Kelvin modes (ω_A, k_A, m_A) and (ω_B, k_B, m_B) satisfying

$$\omega_A = \omega_B, \quad k_A = k_B, \quad |m_A - m_B| = 3. \quad (4.4)$$

Kelvin modes of the Lamb-Oseen vortex have been analysed by Fabre *et al.* (2006). In a viscous fluid, Kelvin modes are always damped ($\text{Im}(\omega) < 0$). Some of the Kelvin modes become neutral as the Reynolds number goes to infinity. But other continues to exhibit a large damping, which is associated with the presence of a critical layer (Sipp & Jacquin 2003). This feature makes the Lamb-Oseen vortex very different from the Rankine vortex for which there is no critical layer damping.

4.2.1. Large- k asymptotic prediction of the Kelvin modes

Le Dizès & Lacaze (2005) have developed an asymptotic theory using WKB analysis to describe the various types of Kelvin modes that can be obtained in the infinite Reynolds number and large axial wavenumber limit. For the Lamb-Oseen vortex, they found two types of neutral modes: regular neutral core modes where no critical point is present, and singular neutral core modes for which a critical point is present on the real-axis but the critical layer damping is asymptotically small. They showed that the frequency range of each mode can be obtained by analyzing the three functions $\omega_{\pm}(r)$ and $\omega_c(r)$ defined by

$$\omega^{\pm}(r) = m\Omega_0(r) \pm \sqrt{2\Omega_0(r)\zeta_0(r)}, \quad (4.5)$$

$$\omega_c(r) = m\Omega_0(r). \quad (4.6)$$

The functions $\omega_{\pm}(r)$ are known as the epicyclic frequencies. They define the upper and lower bounds of the frequency range within which regular neutral core modes (blue regions in figure 7) can exist at a given radial location r . Within this frequency range, the modes exhibit oscillatory behavior for radial positions less than r and decay exponentially beyond that point. The function $\omega_c(r)$, referred to as the critical frequency curve, gives the frequency at which a critical point occurs at r . Regular modes cannot exist at these critical frequencies. However, the damping caused by the critical layer can become asymptotically small if the critical point for a given mode lies at a very large value of r , far from the region where the mode behaves

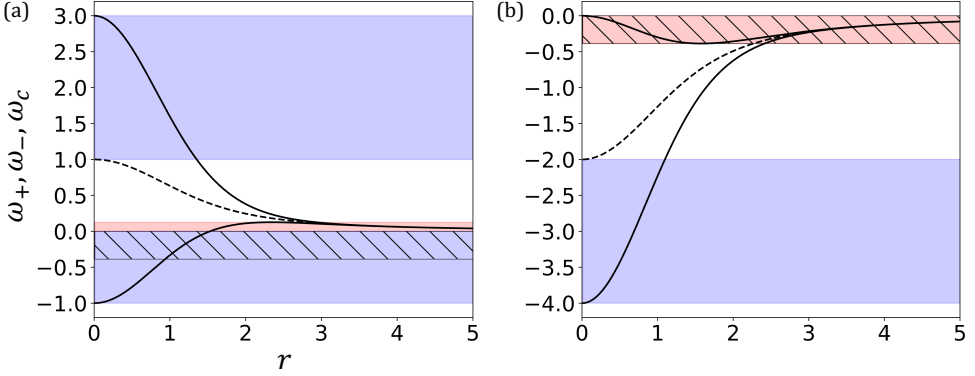


Figure 7: Plot of the epicyclic frequencies ω^+ , ω^- (solid) and the critical frequency ω_c (dashed) as a function of the radial coordinate r ; (a) $m = 1$ (b) $m = -2$; in each figure, the blue regions (resp. red regions) indicate the frequency intervals of regular neutral core modes (resp. singular neutral core modes); the hatched region indicates the frequency interval where resonance between $m = 1$ and $m = -2$ modes is possible.

neutrally. Such modes are called singular neutral core modes (red regions in figure 7). For each azimuthal wavenumber m , one can determine the corresponding frequency intervals in which these behaviors occur. For a more detailed explanation, readers are referred to Le Dizès & Lacaze (2005). The condition of resonance can therefore be analyzed by looking at the possible overlap of these frequency intervals for a couple of azimuthal wavenumbers m and $m + 3$. This analysis leads to a unique possibility: only the couple $(m_A, m_B) = (1, -2)$ (and $(m_A, m_B) = (-1, 2)$ by symmetry) exhibits a frequency overlap. It corresponds to the frequency interval $-0.387 < \omega < 0$, where $m_A = -2$ singular core modes and $m_B = 1$ regular core modes both exist, as shown in figure 7.

4.2.2. Numerical determination of the Kelvin modes

The Kelvin modes can also be obtained by numerically solving the eigenvalue problem (4.3), and we use these numerically computed modes for the remainder of the analysis. Our numerical solver employs a Chebyshev spectral collocation method, following the approach of Fabre & Jacquin (2004). The eigenvalue problem defined in the domain $0 < r < \infty$ is extended to $-\infty < r < \infty$ and mapped onto a contour in the complex- r plane. It is then solved in the Chebyshev domain $(-1, 1)$ using $2(N + 1)$ collocation points. A resolution of $N = 200$ is found to be sufficient. For the inviscid limit, we adopt a complex mapping function, similar to the one used by Fabre & Jacquin (2004), defined as

$$r = \frac{H\xi}{1 - \xi^2} + i \frac{A\xi}{\sqrt{1 - \xi^2}}, \quad (4.7)$$

where the parameter H controls the radial spreading of the collocation points, and the parameter A determines the inclination of the contour in the complex plane. We also take advantage of the parity properties of the eigenfunctions. For odd values of m , we express \tilde{w} and \tilde{p} using odd polynomials, and \tilde{u} and \tilde{v} using even polynomials. Conversely, for even values of m , \tilde{w} and \tilde{p} are represented using even polynomials, while \tilde{u} and \tilde{v} are expressed using odd polynomials.

The above procedure has been done for the two azimuthal wavenumbers $m_A = 1$ and $m_B = -2$ and a wavenumber k varying between 0 and 10 at $Re = 10^4$. The result gives

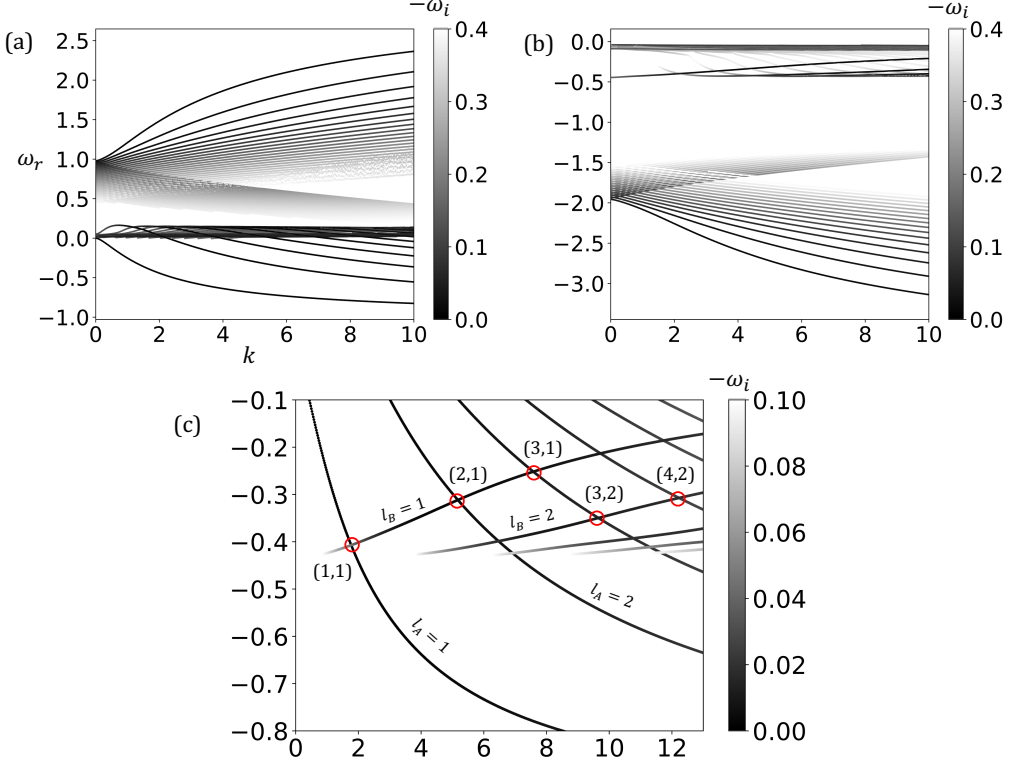


Figure 8: Dispersion curves of the Kelvin modes, obtained by solving the eigenvalue problem in (4.3) on the real axis for (a) $m_A = 1$ and (b) $m_B = -2$ at $Re = 10^4$. The real part of the frequency, ω_r , is plotted against k , while the damping is represented by the greyscale intensity of $-\omega_i$, the imaginary part of the frequency. (c) Resonant Kelvin modes of the unstrained Lamb-Oseen vortex at $Re = 10^4$, identified at the crossing points of the dispersion curves. Modes with positive growth rates at $Re = 10^4$ are circled in red, with their corresponding branch indices indicated in brackets.

the complex frequency curves which have been plotted in figure 8(a,b). One clearly sees in these plots the frequency interval where regular and singular core modes were expected from figure 7.

Figure 8(c) displays the crossing points of $m_A = 1$ and $m_B = -2$ branches. As the damping rate of the modes shown in this figure is small, each crossing point corresponds to a (quasi) resonant configuration. The resonant configurations marked with red circles exhibited positive growth rates, while the other resonant modes showed no growth or negligible growth rates due to critical layer damping and volumic viscous damping. A detailed analysis is provided in the subsequent sections. We label the branches of the dispersion curves as (l_A, l_B) where l_A and l_B are the branch labels of $m_A = 1$ and $m_B = -2$ modes respectively.

An interesting observation is that the branches of the dispersion curves for $m = -2$ involved in the resonance correspond to the 'L branches' described in Fabre *et al.* (2006) (see Figures 19 and 20 in that reference). In particular, the first branch in Figure 8(c) for $m = -2$ matches the 'F branch', also known as the *flattening wave*. Modes on this branch with axial wavenumber $k < 3.45$ are reported to experience significant critical layer damping, while modes with larger k behave as regular, weakly damped waves. This trend is also evident here: the first mode labeled (1, 1) shows stronger critical layer damping compared to the

377 modes labeled (2, 1) and (3, 1), which are only weakly damped. The 'F branch' also has an
 378 analogue in the Rankine vortex, where it is referred to as the 'isolated branch' by Eloy &
 379 Le Dizès (2001) and Fukumoto (2003). The branches below the first one are referred to as
 380 'L2 branches'. In our results, the modes labeled (3, 2) and (4, 2) lie in the weakly damped
 381 regions of these L2 branches. Hence, among the resonant modes considered, only (1, 1)
 382 exhibits strong critical layer damping (also see table 1).

4.3. Theoretical expression for the triangular instability growth rate

383 The method for computing the growth rate associated with the resonant coupling of two
 384 Kelvin modes with the triangular straining field is the same as that used for the elliptic
 385 instability. It is based on an asymptotic analysis in the limit of small ϵ . For more details, we
 386 refer the reader to Moore & Saffman (1975).

387 The idea is to consider the perturbation as a combination of two normal modes of azimuthal
 388 wavenumbers m_A and m_B (related by (4.4)) that corresponds at leading order in ϵ to a resonant
 389 configuration of Kelvin modes. We then write

$$391 \quad \mathbf{u} \sim \left(A \tilde{\mathbf{u}}_A(r) e^{i(m_A \theta)} + B \tilde{\mathbf{u}}_B(r) e^{i(m_B \theta)} \right) e^{i(kz - \omega t)}, \quad (4.8)$$

392 where the (real) axial wavenumber k and the (complex) frequency ω of the two modes
 393 are assumed to be close to a resonant point defined by an axial wavenumber k_c and a real
 394 frequency ω_c (corresponding to one of the crossing points shown in figure 8(c)).

395 Substituting (4.8) in (4.1), we get two equations for the components proportional to $e^{im_A \theta}$
 396 and $e^{im_B \theta}$ respectively as

$$397 \quad A \left(\omega \mathcal{L} - k \mathcal{P} + i \mathcal{M}(m_A) - \frac{i}{Re} \mathcal{V}(m_A, k) \right) \tilde{\mathbf{u}}_A = i B \epsilon \mathcal{N}(m_B) \tilde{\mathbf{u}}_B, \quad (4.9)$$

$$398 \quad B \left(\omega \mathcal{L} - k \mathcal{P} + i \mathcal{M}(m_B) - \frac{i}{Re} \mathcal{V}(m_B, k) \right) \tilde{\mathbf{u}}_B = i A \epsilon \overline{\mathcal{N}}(m_A) \tilde{\mathbf{u}}_A, \quad (4.10)$$

399 where $\mathcal{N}(m_B)$ and $\overline{\mathcal{N}}(m_A)$ are obtained by replacing $\partial/\partial\theta$ with im_B and im_A , respectively,
 400 in the \mathcal{N} and $\overline{\mathcal{N}}$ operators given in appendix B. These equations show how the two modes
 401 are coupled by the straining field which is responsible for the terms on the right-hand side of
 402 these equations.

403 The equation giving the complex frequency ω is obtained from an orthogonality condition
 404 with the adjoint resonant Kelvin modes. The eigenfunctions $\tilde{\mathbf{u}}_A^\dagger$ and $\tilde{\mathbf{u}}_B^\dagger$ of these two adjoint
 405 modes are the solutions of the adjoint equation of (4.3) for $(m, k) = (m_A, k_c)$ and $(m, k) =$
 406 (m_B, k_c) , respectively. These adjoint equations are obtained using the scalar product

$$407 \quad \langle \mathbf{u}_1, \mathbf{u}_2 \rangle = \int_0^\infty \mathbf{u}_1^*(r) \mathbf{u}_2(r) r dr, \quad (4.11)$$

408 where '*' denotes the complex conjugate. We have two options for applying the orthogonality
 409 condition: either we consider the inviscid expressions $(\tilde{\mathbf{u}}_A^{(\infty)}, \tilde{\mathbf{u}}_B^{(\infty)})$ and $(\tilde{\mathbf{u}}_A^{\dagger(\infty)}, \tilde{\mathbf{u}}_B^{\dagger(\infty)})$ of the
 410 Kelvin and adjoint modes or we choose their expression for a given (large) Reynolds number.

411 In the first case, upon performing the scalar product of equation (4.9) with $\tilde{\mathbf{u}}_A^{\dagger(\infty)}$ and of

equation (4.10) with $\tilde{\mathbf{u}}_B^{(\infty)}$, we obtain

$$\left(\omega - \omega_A^{(\infty)} - Q_A^{(\infty)}(k - k_c^{(\infty)}) - i \frac{V_A^{(\infty)}}{Re} \right) A = i \epsilon C_{AB}^{(\infty)} B, \quad (4.12)$$

$$\left(\omega - \omega_B^{(\infty)} - Q_B^{(\infty)}(k - k_c^{(\infty)}) - i \frac{V_B^{(\infty)}}{Re} \right) B = i \epsilon C_{BA}^{(\infty)} A, \quad (4.13)$$

where the coefficients $Q_A^{(\infty)}$, $Q_B^{(\infty)}$, $V_A^{(\infty)}$, $V_B^{(\infty)}$, $C_{AB}^{(\infty)}$, $C_{BA}^{(\infty)}$ are given by

$$Q_A^{(\infty)} = \frac{\langle \tilde{\mathbf{u}}_A^{\dagger(\infty)}, \mathcal{P} \tilde{\mathbf{u}}_A^{(\infty)} \rangle}{\langle \tilde{\mathbf{u}}_A^{\dagger(\infty)}, \mathcal{L} \tilde{\mathbf{u}}_A^{(\infty)} \rangle}, \quad Q_B^{(\infty)} = \frac{\langle \tilde{\mathbf{u}}_B^{\dagger(\infty)}, \mathcal{P} \tilde{\mathbf{u}}_B^{(\infty)} \rangle}{\langle \tilde{\mathbf{u}}_B^{\dagger(\infty)}, \mathcal{L} \tilde{\mathbf{u}}_B^{(\infty)} \rangle}, \quad (4.14)$$

$$V_A^{(\infty)} = \frac{\langle \tilde{\mathbf{u}}_A^{\dagger(\infty)}, \mathcal{V} \tilde{\mathbf{u}}_A^{(\infty)} \rangle}{\langle \tilde{\mathbf{u}}_A^{\dagger(\infty)}, \mathcal{L} \tilde{\mathbf{u}}_A^{(\infty)} \rangle}, \quad V_B^{(\infty)} = \frac{\langle \tilde{\mathbf{u}}_B^{\dagger(\infty)}, \mathcal{V} \tilde{\mathbf{u}}_B^{(\infty)} \rangle}{\langle \tilde{\mathbf{u}}_B^{\dagger(\infty)}, \mathcal{L} \tilde{\mathbf{u}}_B^{(\infty)} \rangle}, \quad (4.15)$$

$$C_{AB}^{(\infty)} = \frac{\langle \tilde{\mathbf{u}}_A^{\dagger}, \mathcal{N}(m_B) \tilde{\mathbf{u}}_B^{(\infty)} \rangle}{\langle \tilde{\mathbf{u}}_A^{\dagger(\infty)}, \mathcal{L} \tilde{\mathbf{u}}_A^{(\infty)} \rangle}, \quad C_{BA}^{(\infty)} = \frac{\langle \tilde{\mathbf{u}}_B^{\dagger(\infty)}, \overline{\mathcal{N}}(m_A) \tilde{\mathbf{u}}_A^{(\infty)} \rangle}{\langle \tilde{\mathbf{u}}_B^{\dagger(\infty)}, \mathcal{L} \tilde{\mathbf{u}}_B^{(\infty)} \rangle}. \quad (4.16)$$

The frequency $\omega_A^{(\infty)}$ and $\omega_B^{(\infty)}$ are the inviscid estimates of the frequencies of the resonant Kelvin modes at $k = k_c^{(\infty)}$. They can be expressed as

$$\omega_A^{(\infty)} = \omega_c^{(\infty)} + i \text{Im}(\omega_A^{(\infty)}), \quad \omega_B^{(\infty)} = \omega_c^{(\infty)} + i \text{Im}(\omega_B^{(\infty)}), \quad (4.17)$$

where $\text{Im}(\omega_A^{(\infty)})$ and $\text{Im}(\omega_B^{(\infty)})$ are the critical layer damping rates of both modes.

For the azimuthal wavenumber couple $(m_A, m_B) = (1, -2)$, only the Kelvin mode with azimuthal wavenumber $m_B = -2$ is expected to experience critical layer damping at resonance. In particular, we have $\text{Im}(\omega_A^{(\infty)}) = 0$ for $m_A = 1$ at resonance.

Equations (4.12)-(4.13) with (4.17) give an equation for the complex frequency ω :

$$\left(\omega - \omega_c^{(\infty)} - Q_A^{(\infty)}(k - k_c^{(\infty)}) - i \frac{V_A^{(\infty)}}{Re} \right) \left(\omega - \omega_c^{(\infty)} - i \text{Im}(\omega_B^{(\infty)}) - Q_B^{(\infty)}(k - k_c^{(\infty)}) - i \frac{V_B^{(\infty)}}{Re} \right) = -\epsilon^2 (N^{(\infty)})^2, \quad (4.18)$$

where

$$N^{(\infty)} = \sqrt{C_{AB}^{(\infty)} C_{BA}^{(\infty)}}. \quad (4.19)$$

The growth rate σ is defined as $\text{Im}(\omega)$ and is computed using the equation above. Both modes oscillate with a common resonant frequency given by $\text{Re}(\omega)$. On the left-hand side of equation (4.18), we recognize the dispersion relation for the two resonant modes, A and B, close to the resonant point. More precisely, the left-hand side can be written as $(\omega - \omega_A(k, Re))(\omega - \omega_B(k, Re))$ where $\omega_A(k, Re)$ and $\omega_B(k, Re)$ are the complex frequencies of the two Kelvin modes for a wavenumber k close to k_c and a large Reynolds number. The right-hand side corresponds to the coupling term that is responsible for the instability.

The integrals in the inner products that appear in the coefficients of (4.14), (4.15), and (4.16) are evaluated along a complex path that avoids the critical point associated with

(l_A, l_B)	(1, 1)	(2, 1)	(3, 1)	(3, 2)	(4, 2)
$k_c^{(\infty)}$	1.76	5.18	7.58	9.64	12.22
$\omega_c^{(\infty)}$	-0.407	-0.312	-0.252	-0.35	-0.307
$\text{Im}(\omega_B)$	-0.044	-2.01×10^{-5}	-6.59×10^{-7}	-2.20×10^{-5}	-1.75×10^{-6}
$Q_A^{(\infty)}$	-0.164	-0.077	-0.054	-0.042	-0.033
$Q_B^{(\infty)} \times 10^2$	$2.96 + 1.09i$	$2.93 - 0.73i$	$2.14 - 0.33i$	$1.76 - 0.24i$	$1.53 - 0.16i$
$V_A^{(\infty)}$	-5.22	-44.60	-101.37	-148.23	-248.91
$V_B^{(\infty)}$	$-3.16 - 3.27i$	$-31.38 - 0.03i$	$-65.96 + 0.00i$	$-108.92 - 0.11i$	$-175.36 + 0.00i$
$C^{(\infty)}$	$10.94 - 6.56i$	$6.76 + 3.43i$	$-4.38 - 0.81i$	$-0.76 - 11.37i$	$-7.45 + 3.46i$
$C_{AB}^{(\infty)}$	$0.95 + 0.91i$	$2.27 - 2.07i$	$-0.93 + 0.44i$	$0.34 + 1.77i$	$-1.47 - 0.27i$
$N_{BA}^{(\infty)}$	$4.07 + 0.46i$	$4.78 - 0.65i$	$2.13 - 0.27i$	$4.50 - 0.58i$	$3.48 - 0.44i$

Table 1: Values of the parameters of the growth rate equation (4.18) for the resonance of two Kelvin modes of azimuthal wavenumbers $m_A = 1$ and $m_B = -2$ at the different resonant points. Integration is done in the complex plane as explained in the text.

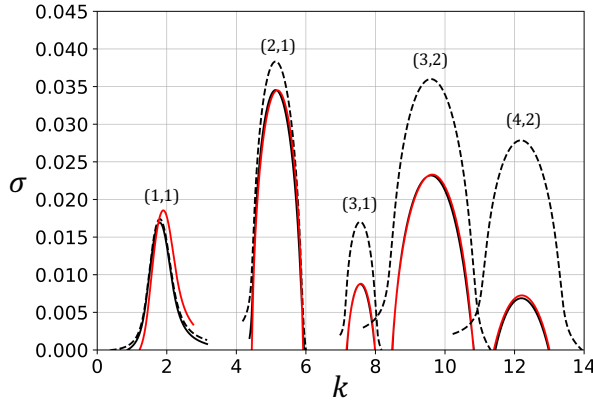


Figure 9: Growth rates σ are plotted against the axial wavenumber k for the resonant modes, based on theoretical predictions. Solid black lines represent results from equation (4.18), while solid red lines correspond to equation (4.20), both computed for $Re = 10^4$. Dashed black lines show results from equation (4.18) in the inviscid limit ($Re = \infty$). The corresponding branch indices are also indicated.

the mode $m = -2$ from below, since it moves in the lower part of the complex plane, as explained in Le Dizès (2004). To achieve this, we use the complex mapping given in (4.7) with parameters $H = 4$ and $A = -0.5$. These values of H and A result in the contour passing slightly below the critical points for all the resonant points corresponding to $m = -2$. The integrals corresponding to $m = 1$ are also computed along this same contour. Since the $m = 1$ modes do not have a critical point, the values of the integrals remain unchanged. In table 1, we provide the values of the parameters appearing in equation (4.18) for all the resonant points that have been identified in figure 8 for the two azimuthal wavenumbers $m_A = 1$ and $m_B = -2$.

An equation for the growth rate can also be obtained using the viscous expression of the

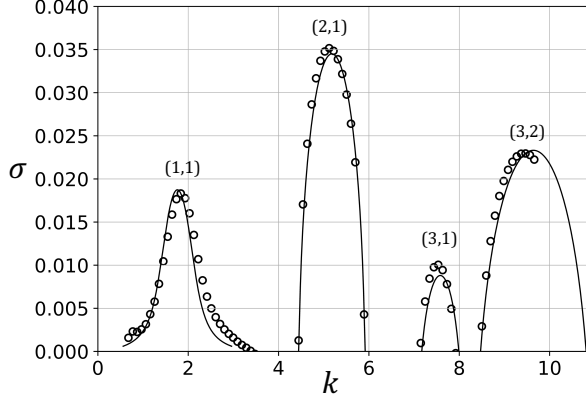


Figure 10: Comparison of growth rates σ against the axial wavenumber k for the first four resonant modes computed using equation (4.20): solid black lines and DNS: circles. Values of the corresponding branch indices are reported.

resonant Kelvin modes. In that case, instead of (4.18), we get the following equation

$$(\omega - \omega_c(Re) - i\text{Im}(\omega_A(Re)) - Q_A(Re)(k - k_c(Re))) \times (\omega - \omega_c(Re) - i\text{Im}(\omega_B(Re)) - Q_B(Re)(k - k_c(Re))) = -\epsilon^2(N(Re))^2, \quad (4.20)$$

where the coefficients now depend on the Reynolds number. Note that the volumic viscous damping terms $iV_A^{(\infty)}/Re$ and $iV_B^{(\infty)}/Re$ in equation (4.18) are now included in the terms $i\text{Im}(\omega_A(Re))$ and $i\text{Im}(\omega_B(Re))$. This second approach has also been used. For the Reynolds number $Re = 10^4$ that we have considered, the results are similar, as can be seen in figure 9. This figure shows the five resonant modes for which a positive viscous growth rate was obtained. In this figure, we have also plotted the growth rate curves obtained from (4.18) for $Re = \infty$. We clearly see that the viscous damping of the modes significantly affects the resonant configurations with the largest wavenumbers.

4.4. Numerical results

In this section, we first describe how growth rates and frequencies are obtained numerically and then compare the results predicted by equation (4.18) or (4.20) with those obtained from DNS. The numerical results are obtained for $Re = 10^4$. Starting from a random initial energy distribution, modes associated with different azimuthal wavenumbers grow exponentially in time if they are unstable. The growth rate is determined as the slope (divided by two) of the logarithm of the energy of the unstable modes. The frequency of the modes is computed by tracking their phase and measuring their rotation rate about the z -axis. The comparison of growth rates is shown in figure 10 for $\epsilon = 0.008$ and k ranging from 0.7 to 10. We observe that the first four unstable modes predicted by the theory within this wavenumber range are also captured in the DNS. The agreement in the growth rates is almost perfect. The values for the frequency and growth rate, obtained by both theory and DNS, for the four unstable modes at their resonant wavenumbers are given in table 2.

In figure 11, we analyse the effect of ϵ on the growth rate curve of the most unstable mode corresponding to $(l_A, l_B) = (2, 1)$. As expected, the growth rate decreases when ϵ is halved, and the agreement between the growth rate curves is excellent, as illustrated in the figure.

The structures and the energy ratio of the contributions from various azimuthal wavenumbers of the unstable modes are displayed in figures 12, 13, 14 and 15. In each figure, the left panel shows the two-dimensional contours of the perturbation axial vorticity field in the

k	(l_A, l_B)	ω_{dns}	ω_{th}	σ_{dns}	σ_{th}	$\sigma_{th}^{(\infty)}$
1.76	(1, 1)	-0.419	-0.406	0.0183	0.0187	0.0174
5.18	(2, 1)	-0.312	-0.312	0.0352	0.0345	0.0383
7.58	(3, 1)	-0.262	-0.252	0.0100	0.0088	0.0170
9.64	(3, 2)	-0.343	-0.350	0.0230	0.0233	0.0360

Table 2: Growth rate σ and real part of the frequency ω of the most unstable mode for different axial wavenumbers k , obtained by DNS and theory (4.20), for $Re = 10^4$ and $\epsilon = 0.008$. The maximum growth rates predicted by (4.18) in the inviscid limit, denoted by $\sigma_{th}^{(\infty)}$, are given in the last column. The chosen axial wavenumbers correspond to the resonant values for the Kelvin modes of azimuthal wavenumbers ($m_A = 1, m_B = -2$) and branch labels (l_A, l_B).

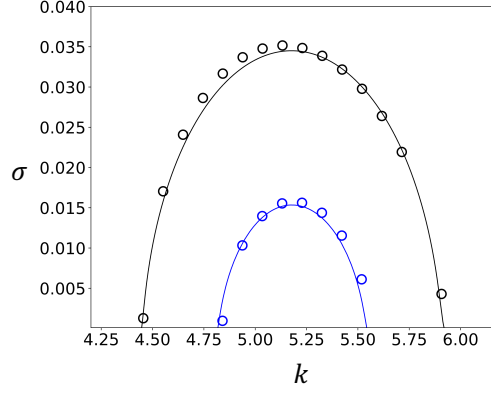


Figure 11: Growth rate σ vs k for the resonant mode with $(l_A, l_B) = (2, 1)$ at $Re = 10^4$. Circles: DNS, solid black lines: theory. Black: $\epsilon = 0.008$; blue: $\epsilon = 0.004$

479 hub vortex, obtained by DNS. The values are divided by $e^{\sigma t_s}$, where σ is the corresponding
480 growth rate and t_s is the simulation time of the snapshot used. In the center panel, we analyze
481 the azimuthal composition of the unstable mode, by computing the energy percentage of each
482 azimuthal component. This decomposition is compared to the theoretical prediction obtained
483 for each resonant configuration. The theoretical energy ratio for mode A, for instance, can be
484 calculated by

$$485 \quad \frac{E_A}{E_A + E_B} = \frac{\int |\tilde{\mathbf{u}}_A|^2 r dr}{\int |\tilde{\mathbf{u}}_A|^2 r dr + (B^2/A^2) \int |\tilde{\mathbf{u}}_B|^2 r dr}, \quad (4.21)$$

486 where $|\tilde{\mathbf{u}}_A|^2 = \tilde{u}_A(r)^2 + \tilde{v}_A(r)^2 + \tilde{w}_A(r)^2$, and (B^2/A^2) can be calculated from equation (4.12)
487 or (4.13). We can see that the unstable modes obtained from DNS are primarily composed of
488 the azimuthal wavenumber pairs $m_A = 1, m_B = -2$ and $m_A = -1, m_B = 2$, with negligible
489 contributions from other azimuthal wavenumbers, as resonance is expected only between
490 these wavenumbers. The energy ratio of the resonant azimuthal wavenumbers aligns well
491 with theoretical predictions, except for the mode corresponding to the branch labels (1, 1),
492 which shows a slight discrepancy. It might be useful to note that the numerically-obtained

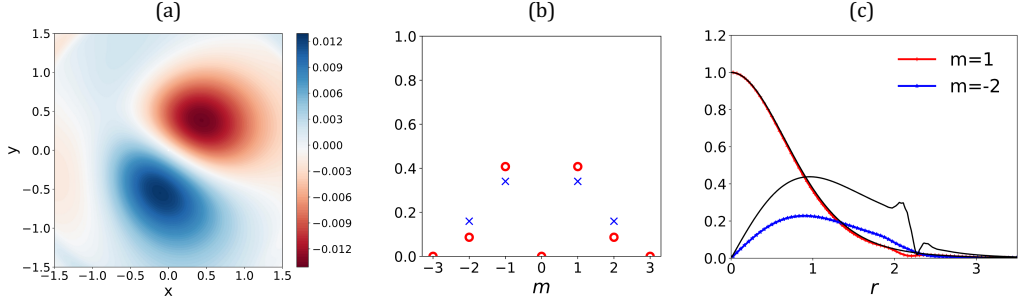


Figure 12: Structure of the resonant combination with $k = 1.76$ for $Re = 10^4$ and $\epsilon = 0.008$; Mode label: $(1,1)$. (a) Contours of the axial vorticity using DNS. (b) Energy ratio; red circles: DNS; blue crosses: theory. (c) Radial structure of the amplitude $|u(r)|$ of radial velocity; colored lines: DNS, black lines: theory.

energy percentages of $m_A = 1$ and $m_B = -2$ are respectively the same as those of $m_A = -1$ and $m_B = 2$. This is due to a certain symmetry that we enforce in the initial random vorticity distribution. Without this symmetry condition, these percentages might differ; however, the mutual energy ratio between the resonant pairs would still be the same. To further validate that the unstable resonant modes obtained from DNS share the same structure as those predicted by theory, the radial distributions of the absolute value of the radial disturbance velocity for both azimuthal wavenumbers are plotted in the right panel, comparing DNS results with theoretical predictions. The radial structures from DNS are extracted by performing a Fourier decomposition of the disturbance fields into components corresponding to different azimuthal wavenumbers. This comparison is conducted by normalizing the amplitude of the $m_A = 1$ azimuthal component to one at the origin in both DNS and theory. A good agreement is also observed here, except for a significant discrepancy in the amplitude of the mode $(1, 1)$ corresponding to $m = -2$. We do not have a definitive explanation for these discrepancies in both the energy ratios and the eigenfunction radial structures for $m = -2$. However, we suspect that they arise from an imperfect representation of the critical layer, particularly strong for $(1, 1)$. Figure 12(c) shows additional oscillations in the theoretical predictions just beyond $r = 2$. These oscillations result from the regularization of the critical layer by viscous effects, which are absent in the numerical results. Therefore, we believe that the observed discrepancy is due to the inaccurate representation of the critical layer. From the left and right panels, it is also evident that modes associated with higher branches exhibit more zeroes in the radial distributions of the disturbance fields.

4.5. Variation of maximum growth rate with Re and ϵ

The theory allows us to easily analyze the effect of ϵ and Re on the instability. Using (4.18), one can compute, for each resonant configuration, the maximum growth rate for any value of ϵ and Re . Figure 16 shows the contours of the maximum growth rate in the (ϵ, Re) parameter plane. For a large range of ϵ ($0 < \epsilon < 0.01$) and Re ($100 < Re < 10^5$), we find that the most unstable mode is always the resonant configuration associated with the branch labels $(l_A, l_B) = (2, 1)$. In particular, the resonant configuration $(1, 1)$ that has the smallest axial wavenumber does not become more unstable than $(2, 1)$ due to the strong critical layer damping of this mode. The contour $\sigma = 0$ represents the marginal stability curve $\epsilon_s(Re)$, above which the resonant configuration $(2, 1)$ is unstable, indicating the presence of the triangular instability. Using (4.18) and the fact that the critical layer damping is negligible

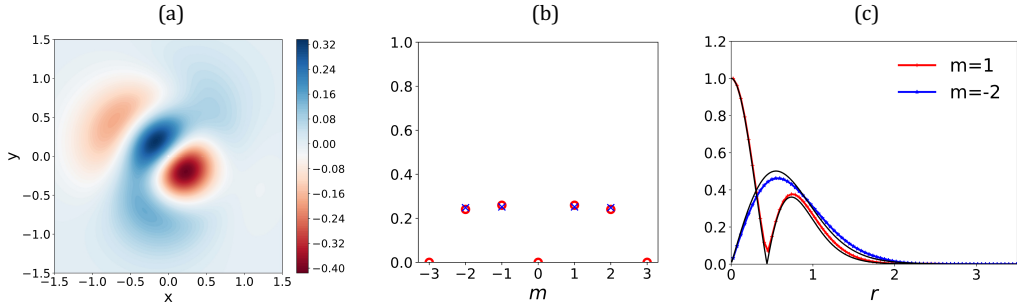


Figure 13: Structure of the resonant combination with $k = 5.18$ for $Re = 10^4$ and $\epsilon = 0.008$; Mode label: (2,1). (a) Contours of the axial vorticity using DNS. (b) Energy ratio; red circles: DNS; blue crosses: theory. (c) Radial structure of the amplitude $|u(r)|$ of radial velocity; colored lines: DNS, black lines: theory.

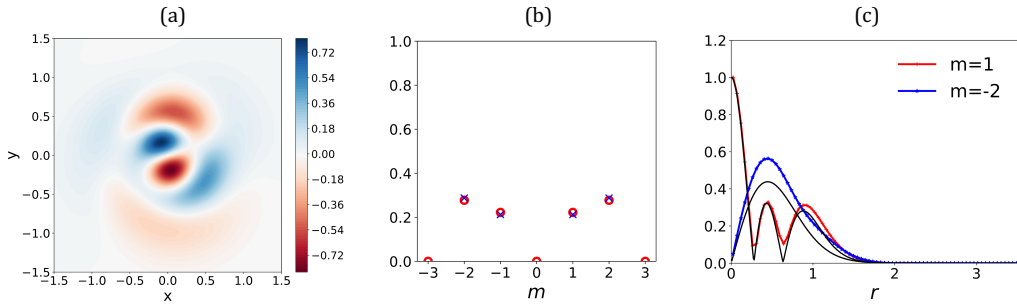


Figure 14: Structure of the resonant combination with $k = 7.58$ for $Re = 10^4$ and $\epsilon = 0.008$; Mode label: (3,1). (a) Contours of the axial vorticity using DNS. (b) Energy ratio; red circles: DNS; blue crosses: theory. (c) Radial structure of the amplitude $|u(r)|$ of radial velocity; colored lines: DNS, black lines: theory.

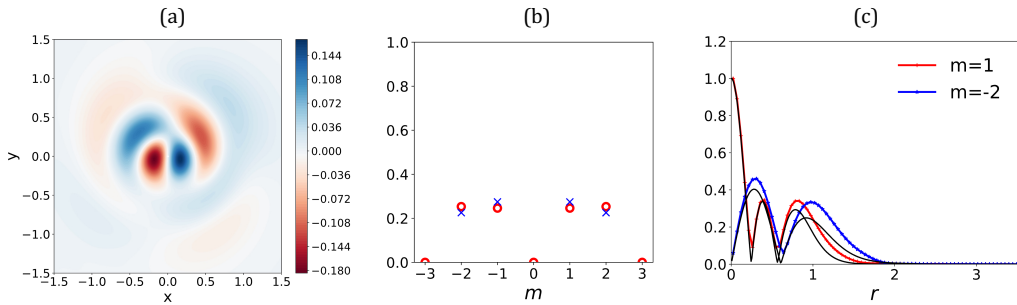


Figure 15: Structure of the resonant combination with $k = 9.64$ for $Re = 10^4$ and $\epsilon = 0.008$; Mode label: (3,2). (a) Contours of the axial vorticity using DNS. (b) Energy ratio; red circles: DNS; blue crosses: theory. (c) Radial structure of the amplitude $|u(r)|$ of radial velocity; colored lines: DNS, black lines: theory.

525 for the resonant configuration (2, 1), this curve can be expressed as

526

$$\epsilon_s(Re) \approx \frac{\sqrt{V_A^{(\infty)} V_B^{(\infty)}}}{N^{(\infty)} Re}, \quad (4.22)$$

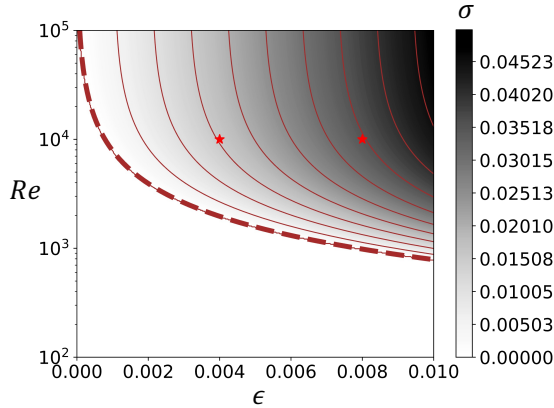


Figure 16: Contours of the maximum growth rate in the (ϵ, Re) parameter space, obtained from theory using equation (4.18). Solid brown lines represent growth rate levels ranging from 0 to 0.045 in increments of 0.005. The marginal stability curve, computed using equation (4.23), is shown as a dashed brown line and corresponds to the zero growth rate level (first brown contour line). Red stars mark the growth rates used in the main test cases: $\sigma = 0.0153$ for $\epsilon = 0.004$ and $\sigma = 0.0345$ for $\epsilon = 0.008$ at $Re = 10^4$.

which gives

$$\epsilon_s(Re) \approx \frac{7.86}{Re} \quad (4.23)$$

using the values provided in table 1 for the resonant configuration (2, 1). Furthermore, the figure illustrates that for practically plausible values of ϵ (towards the right side of the figure), triangular instability can occur at Reynolds numbers as low as $Re \sim 1000$. Similarly, even in cases of very weak straining ($\epsilon < 0.001$), a moderate Reynolds number of $Re \sim 10,000$ can still lead to triangular instability, albeit with small growth rates.

4.6. Comparison with triangular instability in the Rankine vortex

In this section, we briefly compare the characteristics of the triangular instability observed in the Lamb-Oseen vortex with those reported for the Rankine vortex. The latter has been studied theoretically by Eloy & Le Dizès (2001) and their results are used here for comparison.

The most notable difference lies in the absence of a critical layer in the Rankine vortex. This allows resonances for any pair of azimuthal wavenumbers m and $m + 3$, even for asymptotically large m . In contrast, for the Lamb-Oseen vortex, resonance is limited only between $m = 1$ and $m = -2$ (or $m = -1$ and $m = 2$), as critical layer damping suppresses other combinations.

For the Rankine vortex, the maximum growth rate is achieved in the large- m , large- k limit, with $\sigma_{\max}^{(R)} = 49/32\tilde{\epsilon} = 1.53\tilde{\epsilon}$ where $\tilde{\epsilon}$ is related to our external strain rate parameter ϵ by $\tilde{\epsilon} = 9/2\epsilon$. This gives $\sigma_{\max}^{(R)} = 6.89\epsilon$. For the Lamb-Oseen vortex, the highest inviscid growth rate is $\sigma_{\max}^{(L)} = 4.78\epsilon$ for the mode (2, 1) (see Table 1). Alternatively, if one uses the strain rate parameter at the vortex center, which is $\epsilon_0 = (3/2)\epsilon$ for the Rankine vortex, but $\epsilon_0 = s_0\epsilon$ for the Lamb-Oseen vortex, we get $\sigma_{\max}^{(R)} = 4.59\epsilon_0$ and $\sigma_{\max}^{(L)} = 2.70\epsilon_0$. In both cases, the values remain below the maximum growth rate reported for the Rankine vortex. However, focusing only on modes from the $m = 1$ and $m = -2$ resonance, Eloy & Le Dizès (2001) reported $\sigma^{(R)} = 0.95\tilde{\epsilon} = 4.27\epsilon = 2.85\epsilon_0$ for the first principal mode (see Figure 4(b)). This value is comparable to the maximum growth rate found for the Lamb-Oseen vortex, which occurred

for the non-principal mode $(2, 1)$. As shown in this study, the first principal mode is subject to significant critical layer damping and does not become the most unstable mode.

5. Concluding remarks

We have studied the linear instability of a Lamb-Oseen vortex subjected to triangular straining and, for the first time, demonstrated the occurrence of triangular instability in such a vortex, both numerically and theoretically. In our numerical analysis, we modelled the triangular strain field acting on the Lamb-Oseen vortex as being generated by three surrounding satellite vortices with opposite circulation. A 2-D quasi-steady solution was first numerically obtained and then used as the base flow for a 3-D linear stability analysis. The theoretical analysis involved deriving an asymptotic solution for the base flow in the limit of small strain rates, which was shown to accurately describe the numerical solution in the core of the strained vortex. In this framework, the strain rate parameter ϵ was defined as the ratio $(a/R)^3$ where a is the vortex core size, and R is the distance of satellite vortices from the vortex center. By interpreting the triangular instability as a resonance phenomenon similar to that occurring in elliptic instability, we showed that only Kelvin modes with azimuthal wavenumbers $m = 1$ and $m = -2$ (or $m = -1$ and $m = 2$) can resonate with the triangular strain field and drive the instability. This mode selection has been attributed to critical layer damping affecting many of the Kelvin modes in the Lamb-Oseen vortex. In particular, the resonant modes belonging to $m = -2$ exhibit critical layer damping, whereas the $m = 1$ modes are regular and do not undergo any critical layer damping. We derived an explicit expression for the growth rate of the first few resonant modes – corresponding to the intersections of the branches of the two modes with the smallest labels – and compared it with the growth rates obtained numerically. For $Re = 10^4$ and $\epsilon = 0.008$, very good agreement was observed. The structures of the unstable modes obtained from DNS and those predicted by the theory were compared and found to be in excellent agreement in all cases, except for the mode with the smallest axial wavenumber, where the agreement for structures corresponding to $m = -2$ was not perfect due to the imperfect representation of the strong critical layer effect in the theoretical analysis. Using the theory, a complete stability diagram in the (ϵ, Re) parameter plane was also constructed. In addition, we showed that the most unstable mode always corresponds to the resonant configuration formed by the two Kelvin modes with azimuthal wavenumbers $m_A = 1$ and $m_B = -2$, and branch labels $l_A = 2$ and $l_B = 1$, respectively. This mode has an axial wavenumber $k \approx 5.18/a$ and a frequency $\omega \approx -0.312\Omega$, where Ω is the angular velocity at the vortex center.

In this work, we focused on the strained Lamb-Oseen vortex. In applications where the vortices are created by lifting surfaces, vortices also possess an axial flow component. In such cases, a more adequate model would be the Batchelor vortex. As explained in Le Dizès & Lacaze (2005), the characteristics of the Kelvin modes are strongly impacted by the addition of axial flow. Therefore, in a Batchelor vortex, the conditions of resonance are expected to be modified, and other modes with different azimuthal wavenumbers may be excited, as observed in the case of the elliptic instability (Lacaze *et al.* 2007).

By choosing satellite vortices of opposite circulation, we exactly canceled the rotation of the satellite vortices around the central vortex. If the circulation of the satellite vortices were different, the satellite vortices would rotate, causing the induced triangular strain field to rotate as well. This effect is known to impact the base flow. Specifically, if the rotation is in the same direction as the vortex's angular rotation, a critical layer is expected to appear, significantly modifying the strain field structure (Le Dizès 2000). The conditions of resonance would also be modified, potentially suppressing some resonances and creating new ones.

It is also worth emphasizing that our base flow model is 2-D. In wind turbine applications,

if the rotor has 3 blades, the tip vortices generate a strain field on the hub vortex with $m = 3$ azimuthal symmetry. However, tip vortices are helical, meaning induced strain also has helical symmetry and exhibit an axial dependence related to the pitch of the helical structure. It would be interesting to study the impact of this effect on the triangular instability.

Furthermore, it is important to note that the hub vortex is not always a straight vortex on the rotor axis. It may also exhibit a helical structure, depending on the rotor blade design (Durán Venegas & Le Dizès 2019), which makes it sensitive to other short-wavelength instabilities such as elliptic and curvature instabilities (Blanco-Rodríguez & Le Dizès 2016, 2017). The instability of the hub vortex is also expected to compete with the short-wavelength instabilities that develop in the core of the helical satellite vortices, as well as with the long-wavelength instabilities affecting the entire system composed of hub and satellite vortices (Quaranta *et al.* 2015; Durán Venegas & Le Dizès 2019).

Finally, our analysis considered only the linear dynamics associated with the triangular instability. Whether this instability can lead to the destruction of the vortex structure remains an open question, requiring further investigation in the nonlinear regime.

Appendix A. Computation of the base flow parameters from numerical simulations

The circulation (Γ), first-order moments (M_x , M_y), and second-order moments of vorticity (M_{xx} , M_{yy}) for the hub vortex are tracked over time as the simulation progresses, and are computed from the vorticity field ζ as

$$\Gamma = \int_D \zeta \, dxdy, \quad (\text{A } 1)$$

$$M_x = \int_D x\zeta \, dxdy, \quad M_y = \int_D y\zeta \, dxdy, \quad (\text{A } 2)$$

$$M_{xx} = \int_D x^2\zeta \, dxdy, \quad M_{yy} = \int_D y^2\zeta \, dxdy, \quad (\text{A } 3)$$

where these integrals are evaluated over the disk D of radius $0.5R$ around the point where the vorticity reaches its maximum. The core radius of the hub vortex is then computed as

$$a^2 = \frac{M_{xx} + M_{yy}}{\Gamma}. \quad (\text{A } 4)$$

Alternatively, the core radius can be determined by fitting a Gaussian profile to the axisymmetric component of the vorticity distribution. We have verified that the difference between the core radius obtained through these two methods is negligible.

Appendix B. Linear stability analysis - operators and coefficients

The operators appearing in (4.1) are

$$\mathcal{L} = \begin{pmatrix} 1 & 0 & 0 & 0 \\ 0 & 1 & 0 & 0 \\ 0 & 0 & 1 & 0 \\ 0 & 0 & 0 & 0 \end{pmatrix}, \quad (\text{B } 1)$$

$$\mathcal{P} = \begin{pmatrix} 0 & 0 & 0 & 0 \\ 0 & 0 & 0 & 0 \\ 0 & 0 & 0 & 1 \\ 0 & 0 & 1 & 0 \end{pmatrix}, \quad (\text{B } 2)$$

$$\mathcal{M} = \begin{pmatrix} \Omega \frac{\partial}{\partial \theta} & -2\Omega & 0 & \frac{\partial}{\partial r} \\ 2\Omega + r \frac{d\Omega}{dr} & \Omega \frac{\partial}{\partial \theta} & 0 & \frac{1}{r} \frac{\partial}{\partial \theta} \\ 0 & 0 & \Omega \frac{\partial}{\partial \theta} & 0 \\ \frac{\partial}{\partial r} + \frac{1}{r} & \frac{1}{r} \frac{\partial}{\partial \theta} & 0 & 0 \end{pmatrix}, \quad (\text{B } 3)$$

$$\mathcal{V} = \begin{pmatrix} \Delta - \frac{1}{r^2} & -\frac{2}{r^2} \frac{\partial}{\partial \theta} & 0 & 0 \\ \frac{2}{r^2} \frac{\partial}{\partial \theta} & \Delta - \frac{1}{r^2} & 0 & 0 \\ 0 & 0 & \Delta & 0 \\ 0 & 0 & 0 & 0 \end{pmatrix}, \quad (\text{B } 4)$$

where

$$\Delta = \frac{1}{r} \frac{\partial}{\partial r} + \frac{\partial^2}{\partial r^2} + \frac{1}{r^2} \frac{\partial^2}{\partial \theta^2} + \frac{\partial^2}{\partial z^2}. \quad (\text{B } 5)$$

$$\mathcal{N} = \frac{1}{2} \begin{pmatrix} \frac{3f}{r^2} - \frac{3f'}{r} - \frac{3f}{r} \frac{\partial}{\partial r} - \frac{if'}{r} \frac{\partial}{\partial \theta} & -\frac{9if}{r^2} + \frac{2if'}{r} & 0 & 0 \\ -\frac{if'}{r} - if'' & -\frac{3f}{r^2} + \frac{3f'}{r} - \frac{3f}{r} \frac{\partial}{\partial r} - \frac{if'}{r} \frac{\partial}{\partial \theta} & 0 & 0 \\ 0 & 0 & -\frac{3f}{r} \frac{\partial}{\partial r} - \frac{if'}{r} \frac{\partial}{\partial \theta} & 0 \\ 0 & 0 & 0 & 0 \end{pmatrix}, \quad (\text{B } 6)$$

with \overline{N} being the complex conjugate of N .

REFERENCES

- ARENDET, S., FRITTS, D. C. & ANDREASSEN, O. 1998 Kelvin twist waves in the transition to turbulence. *Eur. J. Mech. B Fluids* **17** (4), 595–604.
- ASH, R. L., KHORRAMI, M. R. & GREEN, S. I. 1995 Vortex stability. *Fluid Mechanics and its Applications* **30**, 317–317.
- BAYLY, B. J. 1986 Three-dimensional instability of elliptical flow. *Phys. Rev. Lett.* **57** (17), 2160.
- BLANCO-RODRÍGUEZ, F. J. & LE DIZÈS, S. 2016 Elliptic instability of a curved Batchelor vortex. *J. Fluid Mech.* **804**, 224–247.
- BLANCO-RODRÍGUEZ, F. J. & LE DIZÈS, S. 2017 Curvature instability of a curved Batchelor vortex. *J. Fluid Mech.* **814**, 397–415.
- BRION, V., SIPP, D. & JACQUIN, L. 2007 Optimal amplification of the crow instability. *Phys. Fluids* **19** (11).
- CARNEVALE, G. F. & KLOOSTERZIEL, R. C. 1994 Emergence and evolution of triangular vortices. *J. Fluid Mech.* **259**, 305–331.
- CROW, S. 1970 Stability theory for a pair of trailing vortices. *AIAA J.* **8** (12), 2172–2179.
- DRITSCHEL, D. G. 1998 On the persistence of non-axisymmetric vortices in inviscid two-dimensional flows. *J. Fluid Mech.* **371**, 141–155.
- DURÁN VENEGAS, E. & LE DIZÈS, S. 2019 Generalized helical vortex pairs. *J. Fluid Mech.* **865**, 523–545.
- ELOY, C. & LE DIZÈS, S. 2001 Stability of the Rankine vortex in a multipolar strain field. *Phys. Fluids* **13** (3), 660–676.
- ELOY, C., LE GAL, P. & LE DIZÈS, S. 2000 Experimental study of the multipolar vortex instability. *Phys. Rev. Lett.* **85** (16), 3400.
- ELOY, C., LE GAL, P. & LE DIZÈS, S. 2003 Elliptic and triangular instabilities in rotating cylinders. *J. Fluid Mech.* **476**, 357–388.
- FABRE, D. & JACQUIN, L. 2004 Viscous instabilities in trailing vortices at large swirl numbers. *J. Fluid Mech.* **500**, 239–262.

- FABRE, D., SIPP, D. & JACQUIN, L. 2006 Kelvin waves and the singular modes of the Lamb-Oseen vortex. *J. Fluid Mech.* **551**, 235–274.
- FUKUMOTO, Y. 2003 The three-dimensional instability of a strained vortex tube revisited. *J. Fluid Mech.* **493**, 287–318.
- FUKUMOTO, Y. & HATTORI, Y. 2005 Curvature instability of a vortex ring. *J. Fluid Mech.* **526**, 77–115.
- HATTORI, Y., BLANCO-RODRÍGUEZ, F. J. & LE DIZÈS, S. 2019 Numerical stability analysis of a vortex ring with swirl. *J. Fluid Mech.* **878**, 5–36.
- HATTORI, Y. & FUKUMOTO, Y. 2003 Short-wavelength stability analysis of thin vortex rings. *Phys. Fluids* **15** (10), 3151–3163.
- HOPFINGER, E. J. & VAN HEIJST, G. J. F. 1993 Vortices in rotating fluids. *Ann. Rev. Fluid Mech.* **25** (1), 241–289.
- JIMÉNEZ, J., MOFFATT, H. K. & VASCO, C. 1996 The structure of the vortices in freely decaying two-dimensional turbulence. *J. Fluid Mech.* **313**, 209–222.
- KERSWELL, R. R. 2002 Elliptical instability. *Ann. Rev. Fluid Mech.* **34** (Volume 34, 2002), 83–113.
- LACAZE, L., RYAN, K. & LE DIZÈS, S. 2007 Elliptic instability in a strained Batchelor vortex. *J. Fluid Mech.* **577**, 341–361.
- LE DIZÈS, S. 2000 Non-axisymmetric vortices in two-dimensional flows. *J. Fluid Mech.* **406**, 175–198.
- LE DIZÈS, S. 2004 Viscous critical-layer analysis of vortex normal modes. *Stud. Appl. Math.* **112** (4), 315–332.
- LE DIZÈS, S. & LACAZE, L. 2005 An asymptotic description of vortex Kelvin modes. *J. Fluid Mech.* **542**, 69–96.
- LE DIZÈS, S. & LAPORTE, F. 2002 Theoretical predictions for the elliptical instability in a two-vortex flow. *J. Fluid Mech.* **471**, 169–201.
- LE DIZÈS, S. & VERGA, A. 2002 Viscous interaction of two co-rotating vortices before merging. *J. Fluid Mech.* **467**, 389–410.
- LELE, S. K. 1992 Compact finite difference schemes with spectral-like resolution. *J. Comput. Phys.* **103** (1), 16–42.
- LEWEKE, T., LE DIZÈS, S. & WILLIAMSON, C. H. K. 2016 Dynamics and Instabilities of Vortex Pairs. *Ann. Rev. Fluid Mech.* **48** (Volume 48, 2016), 507–541.
- LEWEKE, T. & WILLIAMSON, C. H. K. 1998 Cooperative elliptic instability of a vortex pair. *J. Fluid Mech.* **360**, 85–119.
- LEWEKE, T. & WILLIAMSON, C. H. K. 2011 Experiments on long-wavelength instability and reconnection of a vortex pair. *Phys. Fluids* **23** (2).
- MEUNIER, P. & LEWEKE, T. 2005 Elliptic instability of a co-rotating vortex pair. *J. Fluid Mech.* **533**, 125–159.
- MOFFATT, H. K., KIDA, S. & OHKITANI, K. 1994 Stretched vortices – the sinews of turbulence; large-Reynolds-number asymptotics. *J. Fluid Mech.* **259**, 241–264.
- MOORE, D. W. & SAFFMAN, P. G. 1975 The instability of a straight vortex filament in a strain field. *Proc. R. Soc. Lond. A* **346** (1646), 413–425.
- PIERREHUMBERT, R. T. 1986 Universal short-wave instability of two-dimensional eddies in an inviscid fluid. *Phys. Rev. Lett.* **57** (17), 2157.
- PULLIN, D. I. & SAFFMAN, P. G. 1998 Vortex dynamics in turbulence. *Ann. Rev. Fluid Mech.* **30** (1), 31–51.
- QUARANTA, H. U., BOLNOT, H. & LEWEKE, T. 2015 Long-wave instability of a helical vortex. *J. Fluid Mech.* **780**, 687–716.
- ROSSI, L. F., LINGEVITCH, J. F. & BERNOFF, A. J. 1997 Quasi-steady monopole and tripole attractors for relaxing vortices. *Phys. Fluids* **9** (8), 2329–2338.
- SAFFMAN, P. G. 1995 *Vortex dynamics*. Cambridge University Press.
- SCHAEFFER, N. & LE DIZÈS, S. 2010 Nonlinear dynamics of the elliptic instability. *J. Fluid Mech.* **646**, 471–480.
- SIPP, D. & JACQUIN, L. 2003 Widnall instabilities in vortex pairs. *Phys. Fluids* **15**, 1861–1874.
- SIPP, D., JACQUIN, L. & COSSU, C. 2000a Self-adaptation and viscous selection in concentrated two-dimensional vortex dipoles. *Phys. Fluids* **12** (2), 245–248.
- SIPP, D., JACQUIN, L. & COSSU, C. 2000b Self-adaptation and viscous selection in concentrated two-dimensional dipoles. *Phys. Fluids* **12** (2), 245–248.
- TSAI, C.-Y. & WIDNALL, S. E. 1976 The stability of short waves on a straight vortex filament in a weak externally imposed strain field. *J. Fluid Mech.* **73** (4), 721–733.

725 XU, Y., DELBENDE, I., HATTORI, Y. & ROSSI, M. 2025 A numerical procedure to study the stability of helical
726 vortices. *Theor. Comput. Fluid Dyn.* **39**, 15.